Design of Semiconductor Ternary Quantum Dots with Optimal Optoelectronic Function

Dimitrios Maroudas, Xu Han, and Sumeet C. Pandey
Dept. of Chemical Engineering, University of Massachusetts, Amherst, MA 01003

DOI 10.1002/aic.14118
Published online May 21, 2013 in Wiley Online Library (wileyonlinelibrary.com)

The function of nanometer-size quantum dots (QDs) of ternary compound semiconductors, such as $In_xGa_{1-x}As$ and $ZnSe_{1-x}Te_x$, used in the fabrication of optoelectronic and photovoltaic devices can be optimized by precise tuning of their electronic band gap through control of the QD composition (x) and diameter. Results on compositional distributions in ternary QDs and how they affect the QDs' electronic band gap are reported. A hierarchical modeling approach is followed that combines first-principles density functional theory calculations and classical Monte Carlo simulations with a continuum model of species transport in spherical nanocrystals. In certain cases, the model predicts the formation of core/shell-like structures with shell regions rich in the surface segregating species. A systematic parametric analysis generates a database of transport properties, which can be used to design post-growth thermal annealing processes that enable the development of thermodynamically stable QDs with optimal electronic properties grown through simple one-step colloidal synthesis techniques. © 2013 American Institute of Chemical Engineers *AIChE J*, 59: 3223-3236, 2013

Keywords: computational chemistry (at solid surfaces), computer simulations (MC and MD), mathematical modeling, diffusion, materials

Introduction

Compound semiconductor nanocrystals or quantum dots (QDs) with diameters $d \sim 2$–6 nm are used widely in optoelectronic and photovoltaic device fabrication technologies due to the tunability of their electronic and optical properties by controlling the QD size. Free-standing QDs are spherical nanoparticles. As their size increases beyond $d \sim 5$ nm, they develop well-defined low-Miller-index surface facets and their equilibrium crystal shapes become polyhedral;[1,2] equilibrium morphologies of ZnSe, GaAs, and InAs nanocrystals computed from first principles are shown in Figure 1. QDs of ternary compound semiconductors, such as $In_xGa_{1-x}As$, $ZnSe_{1-x}S_x$, and $ZnSe_{1-x}Te_x$, are particularly interesting for technological applications because their optoelectronic properties also can be tuned by modulating their composition through control of the compositional parameter x. Compositional modulation of ternary QDs used in photovoltaic devices has improved their stability against photodegradation and enhanced their quantum yields.[3] The compositional distribution in such ternary QDs may vary widely ranging from solid solutions, that is, randomly alloyed configurations to phase-separated heterostructures, such as core/shell heteronanocomposites.

The range of applications of core/shell structures of II–VI, III–V, and other compound semiconductors is very broad and includes light-emitting diodes (LEDs), photovoltaic devices, and fluorescent biological labels.[4–8] Such semiconductor core/shell QDs are classified broadly in three types, termed type-I, type-II, and reverse type-I; in each of these types of nanocomposite QDs, the shell serves a different purpose. In type-I QDs, the shell material has a wider band gap than that of the core, which passivates efficiently the surface trap states leading to an increased stability against photodegradation and enhanced photoluminescence (PL) quantum yields. In type-II core/shell QDs, the alignment of the electronic energy levels (bands) of the core and the shell material are staggered, while in reverse type-I core/shell QDs the shell material has a band gap that is narrower than that of the core material. In type-II and reverse type-I QDs, controlling the shell thickness is used to tune the spectral emission.[9,10]

QDs are grown widely using colloidal synthesis techniques, which have the advantage of low-cost synthesis and processing compared to QD growth on substrates under ultrahigh vacuum; colloidal synthesis techniques are solution-based and offer convenient linking to polymers and other organic materials. Such techniques have been used to synthesize core/shell QDs with various III–V and II–VI core and shell materials.[11] Growth of core/shell nanocrystals is typically based on two-step overcoating methods that form interfaces between lattice mismatched core and shell regions; the induced misfit strain may cause formation of defects in the crystalline lattice and electronic band offset realignments. Increasing the elastic strain energy due to misfit by increasing the shell thickness affects the electronic energy levels in the QD and may cause transitions in core/shell QDs from type-I to type-II.[12] On the other hand, synthesizing radially graded

Correspondence concerning this article should be addressed to D. Maroudas at maroudas@ecs.umass.edu.

© 2013 American Institute of Chemical Engineers

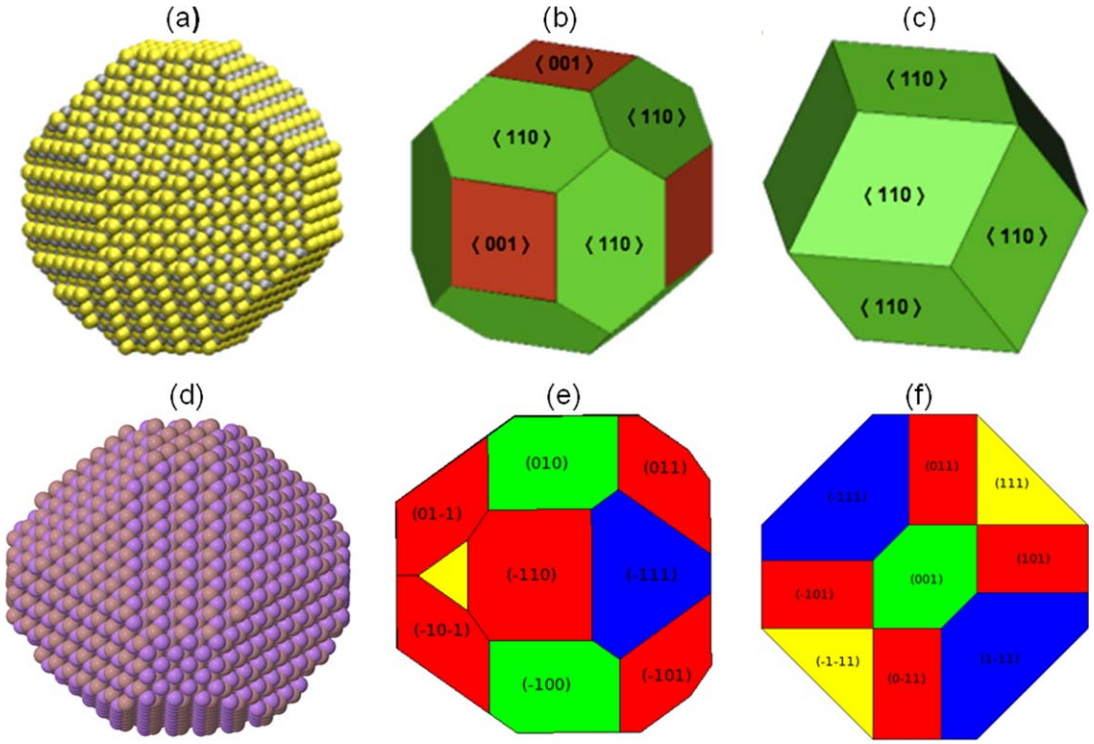

Figure 1. Equilibrium nanocrystal shapes based on *ab-initio*-computed surface energies of low-Miller-index facets of nanocrystals of (a) ZnSe with atoms arranged in a zinc-blende lattice exhibiting well-defined {001} and {110} facets; (b) ZnSe under Se-rich conditions (cubododecahedral); (c) ZnSe under Zn-rich conditions (rhombic dodecahedral); (d) GaAs with atoms arranged in a zinc-blende lattice exhibiting well-defined {001}, {110}, {111}, and $\{\bar{1}\bar{1}\bar{1}\}$ facets in an icosihexahedron morphology; (e) GaAs under As-rich conditions; and (f) InAs under As-rich conditions.

[Color figure can be viewed in the online issue, which is available at wileyonlinelibrary.com.]

ternary alloys with softer confinement potentials has resulted in QDs that exhibit continuous nonblinking PL emission.[13]

Nanocrystal surfaces affect significantly the distribution of constituent atoms in ternary QDs; the atomic species interact with the surface and the nature of this interaction may attract certain atoms to or repel them from the surface of the QD. Moreover, compositional distributions that are kinetically trapped in the nanocrystals during their growth may not be thermodynamically stable. Thermodynamic instabilities undergone by ternary hetero-nanocomposite QDs in devices used for high-temperature applications, such as in photovoltaics and LEDs, have catastrophic consequences for the device function. Thermodynamic stability of such ternary QDs is required to ensure long lifetimes, high performance, and electrical reliability of devices.

The purpose of this study is to develop a continuum model of atomic species transport in ternary QDs, validate it properly, and use it as a predictive tool for designing growth and post-growth processes toward developing QDs with the properties required to guarantee their optimal function in optoelectronic and photovoltaic devices. An important phenomenon underlying species transport in QDs and other nanostructures is drift due to the tendency of certain species to segregate on the nanostructure surfaces; this is properly taken into account in the continuum transport model. The model's validation involves comparison of its predictions with experimental data and results of first-principles-based atomistic simulations; fitting the model to the data and simulation predictions constitutes the model's parameterization. The findings of the analysis contribute to our fundamental understanding of the thermodynamic stability of ternary nanocrystals and the self-assembly of core/shell-like structures in ternary QDs; this self-assembly process is equivalent to the formation of a boundary layer near the QD surface in the concentration of a surface segregating species in the QD. Computation of the electronic band gaps of the QDs as a function of QD composition and its distribution in the QD shows that the key to precise band-gap tunability is the determination of the compositional distribution in the QD at equilibrium.

The remainder of this article is structured as follows. In the next section, we develop a continuum transport model for the distribution of species in ternary QDs accounting for surface segregation in addition to Fickian diffusion. The steady-state and equilibrium species concentration profiles in ternary QDs are calculated according to the continuum transport model in the following section; the model is validated by comparisons of its predictions with first-principles-based predictions of equilibrium compositional distributions in $ZnSe_{1-x}Te_x$ and $In_xGa_{1-x}As$ QDs over a range of composition x and QD diameter according to a hierarchical computational approach combining density functional theory (DFT) calculations and Monte Carlo (MC) simulations. The transient version of the properly parameterized continuum model is used in the subsequent section to analyze the post-growth thermal annealing of the ternary QDs. The effects of the compositional distribution in the QD on its electronic band gap are explored in the ensuing section for $ZnSe_{1-x}S_x$ and $ZnSe_{1-x}Te_x$ QDs. Finally, the most important conclusions of our study are summarized in the last section of the article.

Phenomenological Model of Species Transport in Ternary Semiconductor Nanocrystals

To analyze atomic species transport in ternary semiconductor nanocrystals, we have developed a one-dimensional (1-D) transient model based on a phenomenological theory of surface segregation in spherical ternary nanocrystals. The model can be used to describe interdiffusion kinetics during ternary compound semiconductor nanocrystal annealing[14] at temperature T and the self-assembly of thermodynamically stable nanocrystal heterostructures, such as core/shell-like ternary quantum dots.[15] Here, we employ the model to analyze compositional distributions in ternary nanocrystals of compound semiconductors. These materials include III–V compounds of the type $A_xB_{1-x}Y$, such as $In_xGa_{1-x}As$, and II–VI compounds of the type $ZA_{1-x}B_x$, such as $ZnSe_{1-x}S_x$ and $ZnSe_{1-x}Te_x$; in this notation, A, B, Y, and Z denote atomic species from certain groups of the periodic table. The crystalline semiconductors of interest are characterized by a zinc-blende lattice structure. The zinc-blende lattice consists of two face-centered cubic (fcc) sublattices. In the cases of interest, species Z (i.e., the group-II atomic species in the II–VI compounds under consideration) or Y (i.e., the group-V atomic species in the III–V compounds under consideration) occupy the sites of one of the two fcc sublattices, while species A and B occupy the sites of the other sublattice; therefore, in each nanocrystal, the sites of each sublattice are occupied by atoms of the same group of the periodic table. The statement of the problem under study is to determine the compositional distribution of species A and B in their sublattice throughout the nanocrystal for given T, overall composition expressed by the compositional parameter x, and nanocrystal diameter d.

According to the model, atomic species diffusional transport is governed by the continuity equation

$$\frac{\partial C}{\partial t} = -\nabla \cdot \boldsymbol{J} = \nabla \cdot [-\boldsymbol{u}_d C + D\nabla C] \tag{1}$$

where $C = C_i(r,t)$ is the species concentration field for species i = A or B, $\boldsymbol{J} = \boldsymbol{J}_i(r,t)$ is the flux of species i, where t is time and r is the radial coordinate of the spherical nanocrystal with radius R ($0 \le r \le R$), ∇ is the gradient operator, D is the corresponding species diffusion coefficient, and $\boldsymbol{u}_d$ is the species drift velocity. The source for this drift in the nanocrystal is the thermodynamic driving force, $\boldsymbol{F}$, for surface segregation of species A and B and is expressed as $\boldsymbol{F} = -\nabla U$, where $U = U(r)$ is the interaction potential of the diffusing species (A and B) with the nanocrystal surface. The drift velocity $\boldsymbol{u}_d$ is given by the Nernst–Einstein equation

$$\boldsymbol{u}_d = \frac{D\boldsymbol{F}}{k_B T} = -\frac{D\nabla U}{k_B T} \tag{2}$$

where k_B is Boltzmann's constant. The species-surface interaction potential can be expressed as

$$U(r) = \pm \frac{A_s}{(R-r)^3} \tag{3}$$

where A_s is a metric of the strength of the driving force for surface segregation. The sign in the right-hand side of Eq. 3 is positive or negative if the interaction is repulsive or attractive, respectively. The form of the interaction potential U in Eq. 3 is based on elasticity theory; specifically, we use the solution to the problem of elastic interaction between a center of dilatation in an elastically isotropic medium and a surface layer of finite thickness[16–18] and express it in the spherical geometry of the nanocrystal. In Eq. 3, $R - r$ is the distance of the diffusing species from the nanocrystal surface; we use $R = d/2 + r_0$, where r_0 is a characteristic length introduced because Eq. 3 does not attempt to capture the limit $d/2 - r = 0$ and is valid only for $R - r \ge r_0$. The introduction of r_0 prevents a singularity in the interaction potential at $r = d/2$. We take r_0 to be comparable to the interplanar distance in the nanocrystal lattice, $r_0 \sim 0.2$ nm (and equal to 0.2 nm in this study). It should be mentioned that the characteristic length r_0 plays a role analogous to that of the dislocation core radius, R_0, in dislocation theory for preventing an elastic singularity to occur right at the location of a dislocation line in an elastic continuum,[19] by setting the range of validity of the elastic theory up to a distance R_0 from the dislocation line. In our case, the defect in the elastic continuum is not a 1-D dislocation, but a two-dimensional (2-D) free surface and the characteristic length r_0 sets the range of validity of the elastic theory up to a distance r_0 from the surface in the direction normal to the surface. Dislocation core radii are typically taken to be on the order of the interplanar distance in the crystalline lattice,[19] which also is the metric that we have used in choosing the size of r_0 in this study.

The use in the above equations of a spherical nanocrystal morphology, as opposed to the detailed faceted polyhedral shapes of Figure 1, has been validated by comparison of equilibrium compositional distributions computed through atomistic simulations for different nanocrystal shapes.[1] Equation 1 assumes that the nanocrystal surface is stationary; the velocity of the moving surface should be accounted for if this model is to be extended to the analysis of compositional distributions during the growth of such nanocrystals. We also make a few simplifying assumptions. The diffusivities of the atomic species A and B in the nanocrystal are taken to be practically equal, that is, we use a common diffusivity D for diffusion of atoms from the same group in the zinc-blende lattice of the ternary QD. We also take the surface-segregation strength parameters, A_s, of species A and B in Eq. 3 to be equal, but the interaction with the nanocrystal surface is attractive for A and repulsive for B.[20] We apply a symmetry condition at the spherical nanocrystal center and, as there is no escape of species from the nanocrystal surface during annealing, a boundary condition of zero radial flux at the nanocrystal surface

$$\left.\frac{\partial C}{\partial r}\right|_{r=0} = 0 \quad \text{and} \quad \boldsymbol{J} \cdot \hat{\mathbf{r}}\big|_{r=R} = [\boldsymbol{u}_d(R) \cdot \hat{\mathbf{r}}]C(R) - D\left.\frac{\partial C}{\partial r}\right|_{r=R} = 0 \tag{4}$$

where $\hat{\mathbf{r}}$ is the unit vector in the radial direction. The proper initial condition should be specified for each annealing experiment. For example, for an initial core/shell configuration

$$C_A(r,0) = \begin{cases} C_0, & r \in [0, R_c] \\ 0, & r \in (R_c, R] \end{cases} \text{ and } C_B(r,0) = \begin{cases} 0, & r \in [0, R_c] \\ C_0, & r \in (R_c, R] \end{cases} \tag{5}$$

which corresponds to an A/B core/shell configuration (i.e., an AY/BY or a ZA/ZB core/shell configuration of the ternary nanocrystal composition) with R_c being the radius of the core. Equations 1–5 formulate a well-posed boundary-value problem (BVP) for the concentration fields of A and B in the nanocrystal. The 1-D nature of the model, that is, the assumption that there is only radial dependence of C, stems from the driving force for species transport in the nanocrystal, which exists in the radial direction only; this also is evident from the initial and boundary conditions, Eqs. 4 and 5, of the BVP.

Next, we express the differential operators of Eqs. 1 and 2 in spherical coordinates and introduce the dimensionless variables $\eta \equiv r/R$ with $0 \le \eta < 1$, $\Theta \equiv C/C_0$, and $\tau \equiv Dt/R^2$ into the BVP of Eqs. 1–5 to derive the dimensionless form of the BVP. To express this dimensionless form, we also define the drift Peclét number, Pe, as

$$Pe \equiv \frac{u_{d,\max} R}{D} \tag{6}$$

where $u_{d,\max}$ is the velocity scale taken to be equal to the maximum drift velocity; Pe has its usual meaning[21] with drift being used instead of convection. From Eqs. 2 and 3, the drift velocity can be expressed as $\boldsymbol{u}_d = u_{d,r}\hat{\mathbf{r}}$ with

$$u_{d,r} = \frac{3A_s D}{k_B T (R-r)^4} = \frac{3A_s D}{k_B T R^4} \frac{1}{(1-\eta)^4} \tag{7}$$

The drift velocity of Eq. 7 is a monotonically increasing function of η, reaching its maximum value, $u_{d,\max}$, at the nanocrystal surface, $\eta = \kappa = (d/2)/R$. Equation 7 can then be rewritten as

$$u_{d,r} = u_{d,\max} \frac{(1-\kappa)^4}{(1-\eta)^4} \text{ with } u_{d,\max} = \frac{3A_s D}{k_B T R^4} \frac{1}{(1-\kappa)^4} \tag{8}$$

Combining Eqs. 6 and 8 gives

$$Pe = \frac{3A_s}{k_B T R^3} \frac{1}{(1-\kappa)^4} \tag{9}$$

Introducing the above dimensionless variables and parameter into Eqs. 1–3 gives the dimensionless governing equation for the concentration field, $\Theta = \Theta_A(\eta,\tau)$ or $\Theta_B(\eta,\tau)$

$$\frac{\partial \Theta}{\partial \tau} = \frac{\partial^2 \Theta}{\partial \eta^2} + \frac{2}{\eta}\frac{\partial \Theta}{\partial \eta} - Pe\frac{(1-\kappa)^4}{(1-\eta)^4}\frac{\partial \Theta}{\partial \eta} - 2Pe\frac{(1-\kappa)^4(1+\eta)}{\eta(1-\eta)^5}\Theta \tag{10}$$

Similarly, Eq. 4 gives the dimensionless boundary conditions

$$\left.\frac{\partial \Theta}{\partial \eta}\right|_{\eta=0} = 0 \quad \text{and} \quad \left.\frac{\partial \Theta}{\partial \eta}\right|_{\eta=\kappa} - Pe\Theta(\kappa,\tau) = 0 \tag{11}$$

and Eq. 5 yields the dimensionless initial condition

$$\Theta_A(\eta,0) = \begin{cases} 1, & \eta \in [0,\kappa_1] \\ 0, & \eta \in (\kappa_1,\kappa] \end{cases} \text{ and } \Theta_B(\eta,0) = \begin{cases} 0, & \eta \in [0,\kappa_1] \\ 1, & \eta \in (\kappa_1,\kappa] \end{cases} \tag{12}$$

In Eqs. 11 and 12, the surface location is at $\eta = \kappa$ and the location of the initial core/shell interface is at $\eta = \kappa_1 \equiv R_c/R$.

The above 1-D transient model, Eqs. 9–12, gives a very satisfactory description of interdiffusion kinetics in ternary QDs,[14] as well as of the compositional distributions in the QDs at equilibrium.[15] We will demonstrate this in the subsequent section by comparison with results of first-principles-based atomistic simulations of equilibrium compositional distributions in $ZnSe_{1-x}Te_x$ and $In_xGa_{1-x}As$ QDs and will use these results to predict the corresponding surface segregation strength parameters A_s for the diffusing species. These results will then be used in a later section to predict the evolution of the compositional distributions during annealing experiments.

Self-Assembly of Core/Shell-Like Structures in Ternary Quantum Dots

We solved the steady-state form of the BVP of Eqs. 1–4 analytically. We employed perturbation theory, which gives a good characterization of the solution structure in limiting values of Pe; these details are not given here, because it is easy to obtain an exact closed-form solution to the problem. According to Eq. 1, the governing equation at steady state is $\nabla \cdot \boldsymbol{J} = 0$. Satisfying the no-flux boundary condition of Eq. 4 implies that the steady-state solution is equivalent to the equilibrium solution, that is, the solution to the equation $\boldsymbol{J} = \mathbf{0}$. Using the flux expression of Eqs. 1–3 gives the equilibrium solution

$$C_i(r) = B_i \exp\left[-\frac{U(r)}{k_B T}\right] \tag{13}$$

where the constant B_i is determined by satisfying the overall mass balance $N_i = \int_0^R C_i(r)\, 4\pi r^2 dr$ for the atomic species i in the nanocrystal. Equation 13 is the well-known Maxwellian atmosphere of "impurities" forming around larger-scale defects, such as dislocations in the crystalline lattice;[22] here, the "impurities" are the diffusing species and the large-scale defect is the surface. Following the dimensionless notation of Eqs. 10–12, Eq. 13 can be rewritten as

$$\Theta_i(\eta) \propto \exp\left[\frac{Pe(1-\kappa)^4}{3(1-\eta)^3}\right] = \exp\left[\frac{A_s}{k_B T (R-r)^3}\right] \tag{14}$$

for a species that is attracted by and segregates on the nanocrystal surface. It should be noted that the results of the perturbation analysis also give the solution of Eq. 14. For $Pe \ll 1$, the regular-perturbation solution in the form of a Pe-power-series expansion is equal to the Taylor-series expansion of the Maxwellian atmosphere of Eq. 14. For $Pe \gg 1$, the singular-perturbation solution in the form of two matched asymptotic expansions also matches exactly the Maxwellian atmosphere of Eq. 14.

The equilibrium solution of Eq. 14 is plotted in Figure 2 for a ternary QD of $d = 3.8$ nm. In the absence of surface

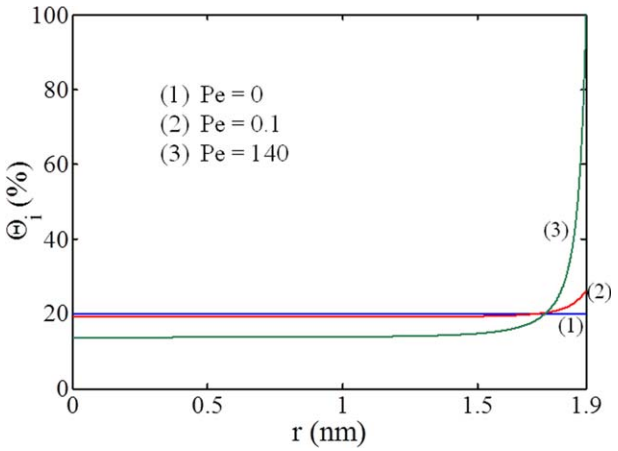

Figure 2. Equilibrium concentration profiles in ternary QDs of $d = 3.8$ nm for $Pe = 0$, $Pe = 0.1$, and $Pe = 140$ according to the Maxwellian-atmosphere solution of Eq. 14.

The profiles range from uniform throughout the nanocrystal at $Pe = 0$ to the formation of a boundary layer near the nanocrystal surface at $Pe = 140$. [Color figure can be viewed in the online issue, which is available at wileyonlinelibrary.com.]

segregation, $A_s = 0$ and Eq. 9 gives $Pe = 0$, which results in a uniform species distribution throughout the nanocrystal. When the species tendency for surface segregation is weak, Eq. 9 gives $Pe \ll 1$ for a low segregation strength A_s, resulting in a species distribution that is just a perturbation from the uniform distribution characterized by an increased species concentration in the near-surface region of the nanocrystal. For a strong tendency for species segregation on the nanocrystal surface, however, the higher segregation strength A_s gives $Pe \gg 1$ and causes the formation of a concentration boundary layer near the nanocrystal surface. This boundary-layer formation has important implications for the design and synthesis of ternary QDs for optoelectronics and photovoltaics. It means that surface segregation drives the assembly of core/shell-like nanocrystals, that is, equilibrium configurations with a core region that is deficient in the segregating species and a shell region near the surface that is rich in the segregating species. Therefore, for ternary QDs with strongly segregating species, Pe can be tailored to determine the shell thickness of the core/shell-like QD. The core and shell regions are separated by a graded "interface" expressed by the smooth and continuous concentration increase near the edge of the boundary layer.

For $Pe \gg 1$, scaling analysis within the boundary layer[21] gives for the boundary-layer thickness δ

$$\frac{\delta}{R} \sim Pe^{-1} \text{ or } \delta \sim \frac{R}{Pe} \tag{15}$$

Combining Eqs. 15 and 9 gives

$$\delta \sim \frac{k_B T(1-\kappa)^4 R^4}{3A_s} = \frac{k_B T r_0^4}{3A_s} \tag{16}$$

Equation 16 implies that, for a ternary QD with a strongly segregating species ($Pe \gg 1$) at given T, increasing the segregation-strength parameter A_s leads to formation of core/shell-like structures with thinner shell regions; A_s is a thermodynamic property of the ternary system and, therefore, $A_s = A_s(x, T)$ in the notation used for the cases examined here. This capability to control the shell thickness of the QD through control of the concentration boundary-layer thickness by tailoring Pe in the $Pe \gg 1$ regime is highlighted in Figure 3.

The predictions of the continuum transport model at steady state and at equilibrium, Eqs. 13 and 14, were validated by comparisons with results from a systematic protocol of first-principles-based atomistic simulations. Fitting the Maxwellian atmosphere of Eq. 14 to the equilibrium concentration profiles computed by the atomistic simulations is then used to determine the values of the segregation-strength parameter A_s for various QD sizes and compositions. Here, we give a brief review of the atomistic simulation methods and results, and focus on using these results for the derivation of the parameters A_s and Pe required for closing the equations of the continuum transport model, Eqs. 9–12.

The atomic-scale computational methods have been described in detail in Refs. 1 and 2. Briefly, we carried out first-principles DFT calculations as implemented in the Vienna *Ab-initio* Simulation Package (VASP)[23,24] employing slab supercells for the computation of Te and In surface segregation energies in thin slabs of $ZnSe_{1-x}Te_x$ and $In_xGa_{1-x}As$ of various low-Miller-index crystallographic orientations of their surface planes. The DFT calculations were implemented within the generalized gradient approximation (GGA)[25] for the exchange and correlation functional, using the projector augmented wave (PAW) method[26,27] for the representation of the ionic cores and plane-wave expansions for the representation of the electronic wave functions. The DFT results were used to properly re-parameterize a classical valence force-field (VFF) description of interatomic interactions in crystals with the zinc-blende lattice structure;[28–30] in the VFF description, bond stretching and bond bending contributions to the crystal energy are accounted for, expressed as an elastic strain energy increase from the energy of an equilibrium configuration.[28–30] Conjugate-gradient minimization of the total energy was carried out with respect to the atomic coordinates in order to obtain the surface segregation energies of the species of interest on the corresponding

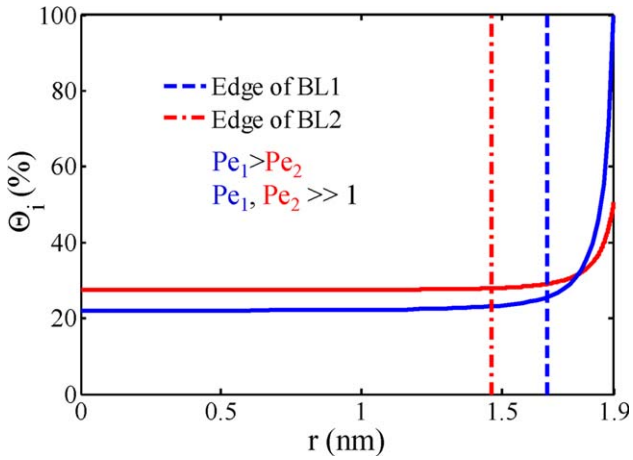

Figure 3. Comparison of concentration boundary-layer (BL) thicknesses in the equilibrium concentration profiles in ternary QDs of $d = 3.8$ nm for $Pe_1 = 80$ (forming BL1) and $Pe_2 = 30$ (forming BL2).

[Color figure can be viewed in the online issue, which is available at wileyonlinelibrary.com.]

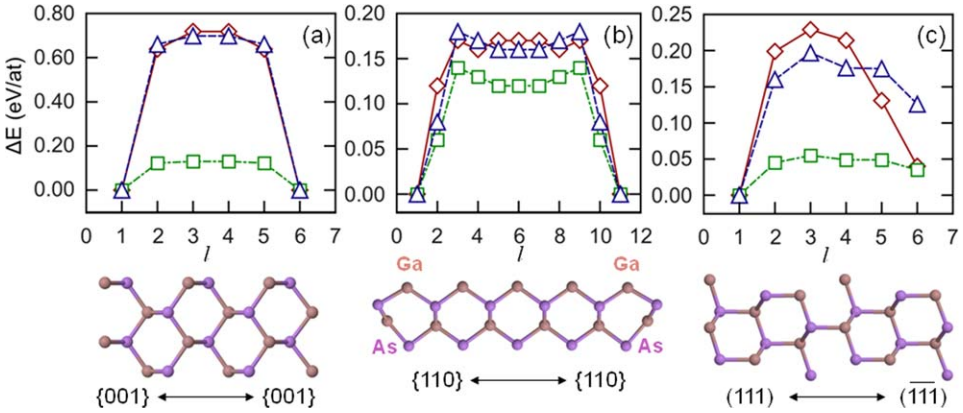

Figure 4. Segregation energy profiles, $\Delta E(l)$, in a thin slab of In:GaAs with (a) two unreconstructed (001) free surfaces, (b) two (110) free surfaces, and (c) one (111) and one $(\bar{1}\bar{1}\bar{1})$ free surfaces.

The slab consists of (a) 11 atomic layers (six when counting only the group-III layers) with $l = 1$ and $l = 6$ being the free-surface layers, (b) 11 atomic layers with the free surfaces at $l = 1$ and $l = 11$, and (c) six group-III layers with the free surfaces at $l = 1$ and $l = 6$. The results denoted by open diamonds (solid lines), squares (dot-dashed lines), and triangles (dashed lines) are calculated by employing DFT, the original VFF parameterization, and the re-parameterized VFF, respectively. Views of 44-, 44-, and 48-atom slab supercells are shown on the bottom for slabs of GaAs(001), (110), and (111)-$(\bar{1}\bar{1}\bar{1})$, respectively. [Color figure can be viewed in the online issue, which is available at wileyonlinelibrary.com.]

surfaces; this energy minimization was employed with both DFT and VFF for consistent comparisons and VFF re-parameterization by least-squares fitting of the DFT results. For the full relaxation of the nanocrystals to obtain their equilibrium configurations, we carried out MC simulations with the required energy computations performed according to the DFT-re-parameterized VFF description. Our MC simulations were performed in a constant-concentration isothermal–isobaric ensemble and involved a three-step relaxation process, namely, compositional, structural, and volumetric relaxation; this includes chemical identity switching through Ising-type flips (compositional relaxation), random atomic displacements (structural relaxation), and attempted trials for volume adjustment (volume relaxation). In all steps, the corresponding trials were accepted or rejected according to the Metropolis criterion. These MC simulations constitute a variant of other MC simulation approaches reported in the literature that have been used in the study of surface segregation in metals[31] and semiconductors.[32] In our approach, the different effects of the various levels of MC relaxation can be studied both separately and collectively.

Figure 4 shows computed surface segregation energy profiles for In segregation on GaAs surfaces. The slab supercell models employed in the computations consist of thin slabs of 11–12 atomic layers separated by 12–14 Å of vacuum; specifically, slabs with unreconstructed (001), (110), and (111)-$(\bar{1}\bar{1}\bar{1})$ surfaces were used with 44-, 44-, and 48-atom supercells, respectively. In atoms were used to substitute Ga atoms at different atomic layers in GaAs and the resulting total energy for this substitution was calculated.[2] The segregation energy, $\Delta E(l)$, that drives the segregation process is given by $\Delta E(l) = E^l_{\text{sub}} - E^s_{\text{sub}}$, where E^l_{sub} is the energy required for substituting one Ga atom by one In atom in a given atomic layer, l, and s is used to denote the first surface atomic layer ($l = 1$). ΔE is the energy change accompanying the move of an In atom from the first surface atomic layer into the subsurface slab region with $\Delta E > 0$ meaning an increase in the energy of the system; $|\Delta E(l+1) - \Delta E(l)|/d_1$, where d_1 is the corresponding interlayer spacing in the slab, provides at each l a measure of the local thermodynamic driving force for In surface segregation.

Figure 4a compares $\Delta E(l)$ profiles in a six-Ga-layer slab of In:GaAs with two unreconstructed (001) surfaces computed according to the original and re-parameterized VFF energies and according to DFT; only the group-III atomic layers are counted, with $l = 1$ corresponding to the first surface layer. Figures 4b and 4c show the corresponding segregation energy profiles in 11-Ga-layer and 6-Ga-layer slabs with unreconstructed (110) and (111)-$(\bar{1}\bar{1}\bar{1})$ free surfaces, respectively. The results of Figures 4a–4c show very good qualitative agreement between VFF and DFT and highlight the preference of the In atom to occupy surface sites for each surface orientation examined. Although the original VFF description significantly underestimates the DFT-computed $\Delta E(l)$ results, the re-parameterized VFF captures the DFT results in a very satisfactory quantitative manner. The results for Te segregation in a ZnSe slab show a completely analogous behavior.[1] Consequently, the resulting re-parameterized VFF classical potentials are very well suited for MC simulations of ternary QD relaxation for predicting the equilibrium concentration profiles in the nanocrystals.

Representative results for equilibrium concentration profiles from the MC simulations are shown in Figure 5. Figures 5a and 5b show ensemble-averaged Te and In concentration profiles, $C_{\text{Te}}(r)$ and $C_{\text{In}}(r)$, respectively, in $ZnSe_{1-x}Te_x$ and $In_xGa_{1-x}As$ QDs, respectively, with spherical morphology, $x = 0.2$, and diameter $d \sim 2.8$ nm. The initial configurations used in the MC simulations were randomly alloyed configurations; in the $ZnSe_{1-x}Te_x$ nanocrystals Se and Te atoms occupied randomly chosen group-VI sites with the Zn atoms occupying the group-II sites of a perfect zinc-blende lattice, while in the $In_xGa_{1-x}As$ nanocrystals In and Ga atoms occupied randomly chosen group-III sites with the As atoms occupying the group-V sites of the lattice. C_{Te} and C_{In} are reported as percentages of the group-VI and group-III atoms, respectively, corresponding to different values of the radial coordinate r in the $ZnSe_{1-x}Te_x$ and $In_xGa_{1-x}As$ nanocrystals, respectively. The results highlight the different effects of the various levels of MC relaxation on the compositional distribution in the ternary QDs; the dominant importance of compositional relaxation is evident from these effects. The results indicate that the equilibrium configurations are core/

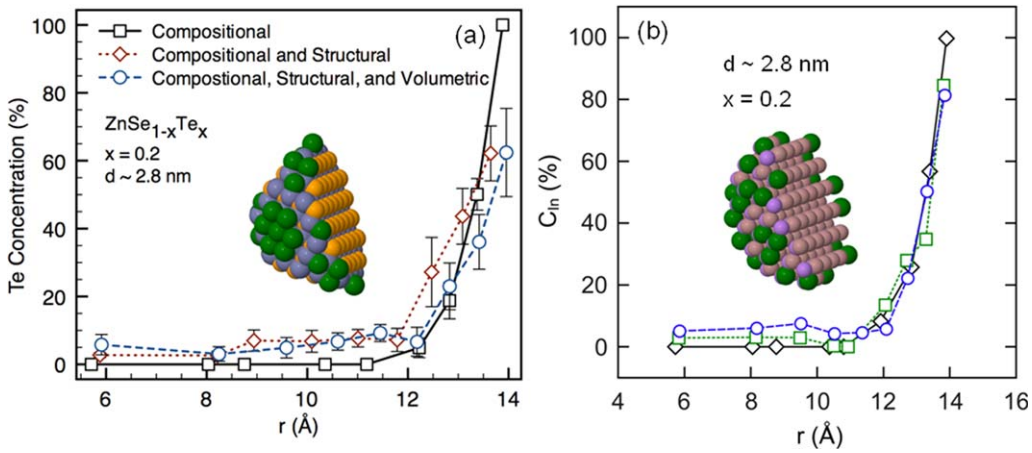

Figure 5. Ensemble-averaged equilibrium (a) Te and (b) In concentration profiles, as functions of the radial coordinate r of the nanocrystal, computed from MC simulations for relaxation of $ZnSe_{1-x}Te_x$ and $In_xGa_{1-x}As$ nanocrystals with $x = 0.2$ and diameter $d \sim 2.8$ nm at different levels of MC relaxation.

Open squares (solid lines), diamonds (dotted lines), and circles (dashed lines) in (a) and open diamonds (solid lines), squares (dotted lines), and circles (dashed lines) in (b) are used to denote concentration profiles obtained by compositional relaxation only, combined compositional and structural relaxation, and full (i.e., combined compositional, structural, and volume) relaxation, respectively. Cross-sectional views of the fully relaxed nanocrystal configurations are shown in the insets. In the relaxed configurations, (a) dark gray (green online), gray (silver online), and light gray (gold online) spheres are used to denote Te, Zn, and Se atoms, respectively, and (b) dark gray (green online), gray (purple online), and light gray (pink online) are used to represent In, As, and Ga atoms, respectively. The error bars in (b) are not shown for clarity; however, they increase with increasing values of r and inclusion of MC trials for structural relaxation. [Color figure can be viewed in the online issue, which is available at wileyonlinelibrary.com.]

shell-like structures with Te-deficient core and Te-rich shell regions in $ZnSe_{1-x}Te_x$ and In-deficient core and In-rich shell regions in $In_xGa_{1-x}As$ with smooth concentration grading between the core and shell regions in both cases. Cross-sectional views of the fully relaxed QD configurations are shown in the insets in Figures 5a and 5b and elucidate in each case the formed core and shell regions that are deficient and rich, respectively, in the surface segregating species. These first-principles-based atomistic simulation results for equilibrium concentration profiles in ternary QDs resemble very strongly the Maxwellian atmospheres of Figure 3.

Indeed, the Maxwellian atmospheres of the continuum transport model provide a very good description of the MC simulation results. This is demonstrated by the results of Figure 6, where the Maxwellian atmospheres of Eq. 14 are used to fit the results of the MC simulations in several cases of relaxed $ZnSe_{1-x}Te_x$ and $In_xGa_{1-x}As$ QD configurations. Specifically, Figures 6a and 6b show results for spherical nanocrystals of $ZnSe_{1-x}Te_x$ with $x = 0.1$ and 0.2, respectively, over the diameter range 2.8 nm $\leq d \leq$ 5.7 nm, while results for $In_xGa_{1-x}As$ spherical nanocrystals over the same range of diameters with $x = 0.1$ and 0.2 are shown in Figures 6c and 6d, respectively. It should be mentioned that the MC simulation results used in the fitting procedure are based only on compositional relaxation of the nanocrystal. This is done because the continuum transport model of Eqs. 1–3 does not account for structural or volume relaxation effects in the nanocrystal. Such relaxation effects can be accounted for in continuum transport models, as discussed in Ref. 33, by accounting for the relaxation volume of the impurity or the constituent atom in the elastic analysis employed in the derivation of the interaction potential U in Eq. 3. Nevertheless, the results of Figure 5 have demonstrated that such structural and volume relaxation effects are not of major importance in determining the equilibrium concentration profiles in the nanocrystals; compositional relaxation effects, that is, configurational contributions to the free energy, dominate with the vibrational excitations due to structural relaxation causing an oscillatory perturbation to the concentration profile that is smoothened by volume relaxation.

The fitting of the MC results of Figure 6 by the Maxwellian-atmosphere solution is very good. In this fitting procedure, there is only one fitting parameter, as is evident from Eq. 14: the segregation strength A_s that determines Pe. The fitting is better for lower values of the overall constituent content, x, simply because both the species transport model, as formulated by Eqs. 1–3, and the elastic analysis, on which Eq. 3 is based, are rigorously valid in the dilute limit. The results of the fitting procedure for all 12 of the datasets (MC profiles) of Figure 6 are listed in Table 1. The derived Pe values exhibit an almost linear dependence on the QD diameter. This can be understood from the definition of Pe, Eq. 9, which implies that, at constant T, $Pe \propto \left(A_s/r_0^4\right)R$. The variation of A_s with the QD diameter is attributed to the changes in the QD surface composition with increasing R and the resulting changes in the elastic parameters that determine A_s.[16–18] Aided by interpolation and extrapolation, these results for A_s can be used for kinetic analyses of drift and diffusion in these ternary systems over a broad range of temperatures, as well as compositions and diameters for the ternary QDs.

In general, our linked DFT/MC atomic-scale modeling of this section provides a rigorous hierarchical approach toward database generation for designing QD post-growth processes aimed at development of QDs with optimal optoelectronic and photovoltaic function. More importantly, the results of this section advocate simple one-step growth strategies (by, e.g., colloidal synthesis) followed by annealing, during which the nanocrystal reaches its equilibrium compositional distribution. The small characteristic diffusional length scales of the QDs guarantee that such equilibration will be achieved over laboratory time scales and motivates the detailed analysis of interdiffusion kinetics in ternary QDs.

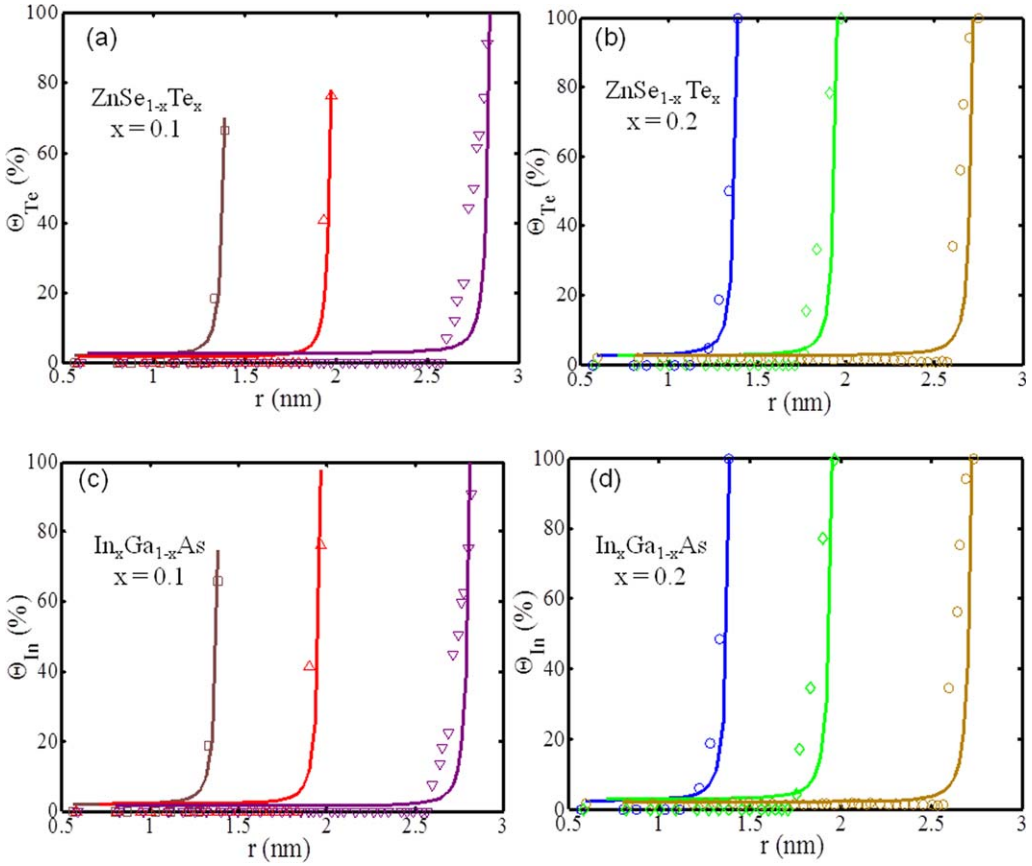

Figure 6. Equilibrium concentration profiles of Te in (a) $ZnSe_{0.90}Te_{0.10}$ and (b) $ZnSe_{0.80}Te_{0.20}$, and In in (c) $In_{0.10}Ga_{0.90}As$ and (d) $In_{0.20}Ga_{0.80}As$ with $d \sim 2.8$ nm, 3.8 nm, and 5.7 nm obtained by MC compositional relaxation (open symbols) and fitting of the MC results according to the Maxwellian-atmosphere solution of Eq. 14 (solid lines).

[Color figure can be viewed in the online issue, which is available at wileyonlinelibrary.com.]

Interdiffusion Kinetics in Ternary Quantum Dots

Having examined the equilibrium compositional distributions in ternary QDs, we now focus on the kinetics that governs the establishment of such compositional distributions, characteristic of self-assembled thermodynamically stable ternary QD configurations; in the QDs considered, this is the kinetics of diffusion of two different species from the same group of the periodic table in the same sublattice of the zinc-blende lattice. The transient BVP of Eqs. 9–12 can be used to interpret experimental measurements of concentration evolution during thermal annealing of ternary QDs and to determine diffusion coefficients and activation barriers, while segregation-strength parameters can be determined also by analysis of atomistic simulation results of equilibrium concentration as was done in the previous section. More importantly, the transient model can be used to make predictions of concentration profile evolution that are important to designing thermal annealing experiments of as grown ternary QDs to aid the self-assembly of thermodynamically stable ternary QDs.

Understanding the thermodynamic stability of alloyed and core/shell (or, in general, heterogeneous) QDs is particularly important, as a certain QD growth strategy may lead to configurations with compositional distributions away from equilibrium. During QD thermal processing or during the service of a device containing such QDs, these as grown configurations will evolve to their equilibrium states, given by the Maxwellian atmospheres as shown in the previous section. The evolution in their compositional distribution may impact the electronic properties of the QDs significantly with respect to those of the as grown configurations. Recent thermal annealing experiments of colloidally synthesized ZnSe/ZnS core/

Table 1. Values of *Pe* and the Segregation-Strength Parameter, A_s, from Fitting the Maxwellian-Atmosphere Solution of Eq. 14 to the MC Simulation Results (Compositional Relaxation Only) of Figure 6 for $ZnSe_{0.90}Te_{0.10}$, $ZnSe_{0.80}Te_{0.20}$, $In_{0.10}Ga_{0.90}As$, and $In_{0.20}Ga_{0.80}As$ Quantum Dots with Diameters $d = 2.8$, 3.8, and 5.7 nm, that is, a Total of 12 Datasets (MC Profiles)

d (nm)	$ZnSe_{1-x}Te_x$	*Pe*	$A_s \times 10^{45}$ (m^5 kg s^{-2})	$In_xGa_{1-x}As$	*Pe*	$A_s \times 10^{45}$ (m^5 kg s^{-2})
2.8	$x = 0.1$	102	1.73	$x = 0.1$	104	1.76
3.8		139	5.33		149	5.71
5.7		205	24.1		350	41.1
2.8	$x = 0.2$	106	1.80	$x = 0.2$	123	2.09
3.8		140	5.37		164	6.29
5.7		212	24.9		363	42.6

For all the simulations analyzed, the temperature is $T = 300$ K.

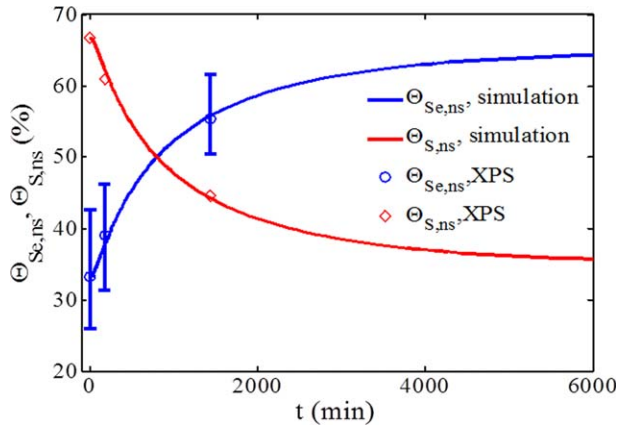

Figure 7. Optimal fitting of XPS data from Ref. 34 (open symbols) for the evolution of the near-surface concentration of Se and S atoms, $\Theta_{Se,ns}$ and $\Theta_{S,ns}$, respectively, during annealing of ZnSe/ZnS core/shell QDs at 90°C over an XPS depth of 0.55 nm from the nanocrystal surface according to numerical solutions (solid lines) of the BVP of Eqs. 10–12.

The error bars indicate the range of the numerical solutions with varying the shell thickness over a range of 0.1 nm about the experimental shell thickness. [Color figure can be viewed in the online issue, which is available at wileyonlinelibrary.com.]

shell QDs have demonstrated such a thermodynamic instability of a core/shell interface.[34] Specifically, ZnSe/ZnS core/shell QDs were synthesized and PL spectroscopy and X-ray photoelectron spectroscopy (XPS) were used on both the as-synthesized and the annealed QDs to determine their properties and near-surface composition as a function of annealing time and temperature. These experimental results emphasized the importance of interdiffusion of Se and S atoms that facilitates the thermodynamic instability and leads to alloying of the initially pure ZnSe core and ZnS shell.[34]

The 1-D transient transport model of Eqs. 1–5 was used successfully in Ref. 14 in simulating the annealing of the ZnSe/ZnS core/shell QDs in the experiments of Ref. 34. First, we review briefly the key results of this thermal annealing modeling to demonstrate the capabilities of the model and, then, we apply the model for new predictions toward designing experiments in other ternary QD systems. Specifically, we review annealing simulations at 90°C of ZnSe/ZnS core/shell QDs with diameter $d = 4.62$ nm, core radius $R_c = 2.0$ nm and shell thickness of 0.31 nm (one monolayer). Figure 7 shows the optimal fitting of the XPS data of Ref. 34 by the results of the model for the near-surface concentration evolution of Se and S atoms, $\Theta_{Se,ns}(t)$ and $\Theta_{S,ns}(t)$, respectively, over an XPS depth $d_{XPS} = 0.55$ nm from the nanocrystal surface.[14] The numerical solutions are shown of the 1-D transient BVP of Eqs. 10–12 (solid lines) for the parameter values that provide the best least-squares fit to the data (open symbols). The near-surface concentrations are expressed as atomic fractions $\Theta_{i,ns} \equiv N_{i,ns}/(N_{Se,ns} + N_{S,ns})$, where i = Se or S and

$$N_{i,ns}(\tau) = \int_{\kappa-\kappa_{XPS}}^{\kappa} \Theta_i(\eta,\tau)\, e^{-(\kappa-\eta)/\lambda} 4\pi\eta^2 d\eta \qquad (17)$$

where $\kappa_{XPS} \equiv d_{XPS}/R$ and the exponential decay $e^{-(\kappa-\eta)/\lambda}$ accounts for the XPS signal intensity decay with a dimensionless inelastic mean free path $\lambda \equiv \Lambda/R$; the dimensional mean free path Λ is taken to be equal to 2.1 nm. The error bars in Figure 7 indicate the range of the numerical solutions with varying the shell thickness of the initial ZnSe/ZnS core/shell configuration from 0.26 to 0.36 nm for an experimental shell thickness of 0.31 nm that gives the results represented by the solid lines. From the results of Figure 7, it is evident that the 1-D transient species transport model, Eqs. 9–12, provides an excellent fitting of the experimental data; the quality of the fitting has been discussed in Ref. 14 and the sufficiency of the dataset has been established. The two fitting parameters involved in this procedure are the diffusion coefficient D through the definition of the dimensionless time τ in Eq. 10 and the segregation-strength parameter A_s through the definition of Pe, Eq. 9. The derived parameter values that result in the best fit of the XPS data are $D = 2.52\times10^{-24}$ m^2/s and $A_s = 8.0\times10^{-56}$ m^5 kgs^{-2}. The derived value of A_s in this case is seen to be 10 orders of magnitude lower than the derived values of A_s from fitting of MC equilibrium profiles (Table 1) in $ZnSe_{1-x}Te_x$ and $In_xGa_{1-x}As$ QDs with species that exhibit strong tendencies for surface segregation. This very low A_s value explains the formation of randomly alloyed configurations during the annealing of $ZnSe_{1-x}S_x$ QDs and the thermodynamic instability of ZnSe/ZnS core/shell QDs.[34]

Having established the capabilities of the transport model of Eqs. 1–5 for QD annealing simulations, we use the model to predict the near-surface concentration evolution in QDs that exhibit a much stronger tendency than $ZnSe_{1-x}S_x$ for species surface segregation. Such QDs include $ZnSe_{1-x}Te_x$ and $In_xGa_{1-x}As$, as established in the previous section. Here, we study the annealing of $ZnSe_{1-x}Te_x$ QDs prepared in various (as grown) initial configurations: these include randomly alloyed QDs, ZnSe/ZnTe core/shell configurations, and ZnTe/ZnSe reverse core/shell configurations. We solve the transient BVP of Eqs. 10–12 numerically.* In the numerical simulations, we use an Adams-Bashforth algorithm with adaptive time step for the time integration of Eq. 10 and a centered finite-difference scheme for the spatial discretization of the concentration field with a fine-resolution finite-difference grid and proper upwinding at the high Pe under consideration.[35] Specifically, we simulated the annealing at 235°C of $ZnSe_{0.80}Te_{0.20}$ QDs with diameter $d = 3.80$ nm; the parameters have been chosen for consistency with preliminary experimental studies in such ternary QDs.

Results from our time-dependent numerical simulations are shown in Figure 8 for the evolution of the Te concentration profile in the ternary QD. The profile evolution for a randomly alloyed $ZnSe_{0.80}Te_{0.20}$ and a ZnTe/ZnSe reverse core/shell configuration is shown in Figures 8a and 8b, respectively. These initial conditions correspond to the uniform distribution at $t = 0$ in Figure 8a and the Heaviside step function at $t = 0$ in Figure 8b that marks the location of the initially abrupt reverse core/shell interface. The Te concentration Θ_{Te} is expressed in terms of the atomic fraction of Te among group-VI species in the nanocrystal. The value of Pe used in these simulations, $Pe = 140$, was taken from Table 1. Consistently with the atomistic simulation results of Figure 5, these dynamical simulation

*The transient BVP of Eqs. 10–12 is linear in $\Theta(\eta,\tau)$ and can be solved analytically. The analytical solution requires the introduction of currently unavailable eigenfunctions in the Fourier-series representation of the evolving concentration profile, that is, precisely the kind of problem that Neal Amundson would love to solve; nevertheless, this is beyond the scope of this article (i.e., outside the materials topical area where this article belongs).

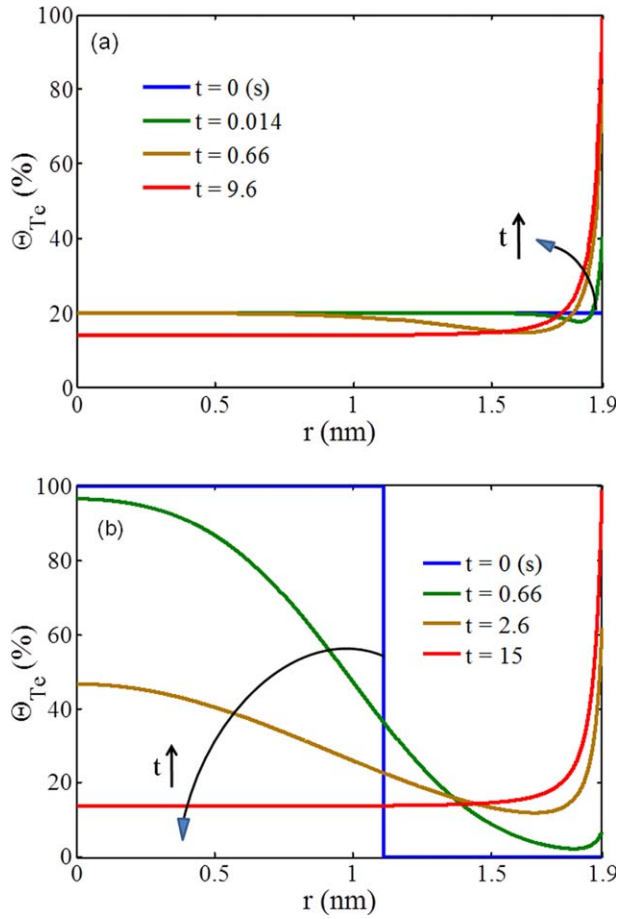

Figure 8. Computed evolution of the Te concentration profile in a ternary $ZnSe_{0.80}Te_{0.20}$ QD from an initial compositional distribution that corresponds to (a) a randomly alloyed configuration and (b) a ZnTe/ZnSe reverse core/shell configuration due to interdiffusion during the thermal annealing of the QD.

[Color figure can be viewed in the online issue, which is available at wileyonlinelibrary.com.]

results demonstrate that the randomly alloyed and reverse core/shell configurations are not stable and that Te and Se interdiffusion leads to the formation of a Te-deficient core region and a Te-rich shell region. We have also shown that ZnSe/ZnTe core/shell configurations with abrupt core/shell interfaces are not stable either, in the sense that the group-VI species interdiffusion generates a graded interface, that is, a core/shell-like structure with a diffuse boundary between the core and the shell regions instead of a sharp interface. In all cases, the evolution of the concentration profiles is followed for over 10 s at the annealing temperature of 235°C, which is a sufficiently long time period for the compositional distributions in the nanocrystal to reach their steady states. All of the long-time profiles (>5 s) of Figure 8 depict the formation of a Te concentration boundary layer at steady state that resembles very closely the Maxwellian atmosphere of Eq. 14. In order to fully quantify the concentrations of Te and Se, we have satisfied the overall mass balance in the $ZnSe_{1-x}Te_x$ nanocrystal, that is, the total numbers of Te and Se atoms in the nanocrystal, N_{Te} and N_{Se}, respectively, are conserved throughout the duration of the annealing. This overall atomic species balance also sets the value of the compositional parameter, x, that is, $x = N_{Te}/(N_{Se} + N_{Te})$; N_{Te} and N_{Se} are equal to the integrals over the spherical nanocrystal volume of the corresponding concentration fields. The tracking of dimensional time in the dynamical simulations requires knowledge of the diffusion coefficient and is discussed below. Finally, the two cases of profile evolution examined in Figure 8 show that the time to steady state is longest for a ZnTe/ZnSe reverse core/shell initial configuration due to the longer diffusional length scales involved in this case: all of the Te is initially in the core and diffuses from the core to the shell region, while all of the Se is initially in the shell and diffuses from the shell to the core region.

Before using these dynamical simulation results in the analysis of the near-surface concentration evolution based on Eq. 17, the validity of the 1-D transient model was confirmed further by comparing its long-time-limit results with the exact solution to the steady-state model that is given by the Maxwellian atmosphere of Eq. 14. These comparisons are shown in Figure 9 for the Te concentration profile in the ternary $ZnSe_{1-x}Te_x$ QD and demonstrate excellent agreement between the numerical predictions, both the long-time-limit transient BVP solution and the steady-state BVP solution, and the exact analytical solution; this confirms the observation made in Figure 8 on the relation of the long-time-limit concentration profiles with the Maxwellian atmosphere: they are exactly equal. Moreover, the long-time-limit dynamical simulation results for the concentration profiles are found to be identical regardless of the initial configuration used in the simulation.

The model predictions for the evolution of the near-surface concentration of the group-VI species, Te and Se, in the ternary QD are shown in Figure 10 for an initial configuration of a reverse core/shell ZnTe/ZnSe QD; the profile evolution, $\Theta_i(\eta, \tau)$ for $i = \text{Te}$, for this initial configuration is given in Figure 8b. In addition to the integration of Eq. 17 with $\Lambda = 1.9$ nm in this case, reporting the evolution of $\Theta_{Te,ns}$ and $\Theta_{Se,ns}$ over dimensional time requires information for the

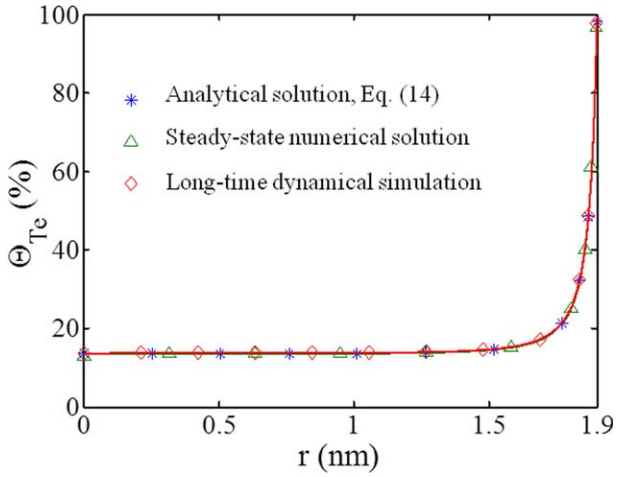

Figure 9. Steady-state Te concentration profile in a ternary $ZnSe_{0.80}Te_{0.20}$ QD reached due to interdiffusional transport during the thermal annealing of the QD from an initial ZnTe/ZnSe reverse core/shell configuration.

The long-time-limit profile according to dynamical simulation, the numerical solution of the steady-state BVP, and the exact analytical solution of the steady-state BVP, Eq. 14, are compared and shown to be in excellent agreement with each other. [Color figure can be viewed in the online issue, which is available at wileyonlinelibrary.com.]

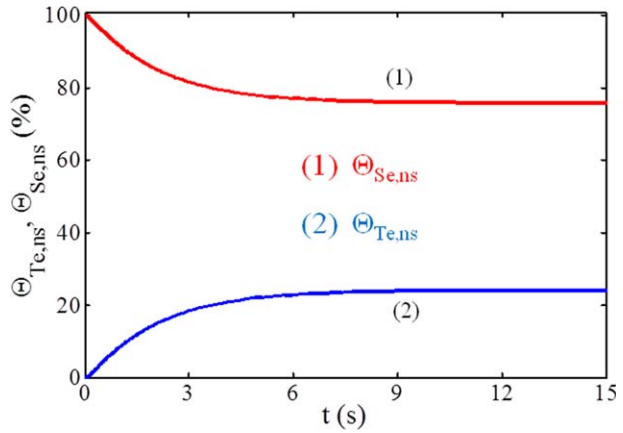

Figure 10. Computed evolution of the near-surface concentration of Se and Te atoms, $\Theta_{Se,ns}$ and $\Theta_{Te,ns}$, respectively, during annealing of ZnTe/ZnSe reverse core/shell QDs at 235°C over an XPS depth of 0.65 nm from the nanocrystal surface.

[Color figure can be viewed in the online issue, which is available at wileyonlinelibrary.com.]

diffusion coefficient D. This information cannot be provided by the equilibrium atomistic simulations of the previous section. In Ref. 14, D was part of the outcome of the fitting procedure of Figure 7 and was based on the availability of XPS (i.e., experimental) data. Also, derivation of D for solid-state diffusion based on atomistic simulation is a very tedious task and requires detailed knowledge of lattice defects, the specific diffusion mechanisms that they mediate in the system of interest, and optimal diffusion pathways for each such mechanism. However, reasonable estimates of D are possible according to the general atomic-level kinetic expression for three-dimensional solid-state diffusion,[21] that is, $D = \Gamma a_h^2/6$, where Γ is the atomic jump frequency and a_h is the atomic hop distance. For diffusion of group-VI species in the nanocrystals under consideration, a_h is taken to be the nearest-neighbor distance between group-VI atoms in the zinc-blende lattice, $a_h = a_0\sqrt{2}/2$ with a_0 being the equilibrium lattice parameter, and atomic hops are thermally activated, that is, Γ is given by an Arrhenius-type expression. Combining the above yields

$$D = \frac{1}{6}\left(a_0\frac{\sqrt{2}}{2}\right)^2 \nu_0 \exp\left(-\frac{E_a}{k_B T}\right) \tag{18}$$

In Eq. 18, ν_0 is the attempt frequency with $\nu_0 \sim 10^{13}$ s^{-1} for most crystalline lattices, $T = 508$ K for the annealing process, and E_a is the thermal activation energy for diffusion of Se or Te in the zinc-blende lattice. Using in Eq. 18, $a_0 = 5.67$ Å for ZnSe and an estimated activation barrier for diffusion of[14] $E_a = 1.25$ eV gives $D = 1.06 \times 10^{-19}$ m^2/s.

This value of D was used in the simulations that yielded the results of Figure 8 and to make dimensional the $\Theta_{i,ns}$ evolution in Figure 10. The results of Figure 10 are valuable in designing annealing experiments to aid thermally the self-assembly of the equilibrium core/shell-like structures of the $ZnSe_{1-x}Te_x$ QDs. For the annealing temperature of 235°C used here, the time to steady state is found to be only a few seconds and the plateau level of the near-surface concentration provides complementary information to the Maxwellian atmosphere for determining the Te-rich shell thickness and the graded interface region of the equilibrium, thermodynamically stable configuration. The very short time to steady state is due to the high annealing temperature and the small diffusional length scale (the QD radius) and should be contrasted with the time to steady state in the annealing experiment of Figure 7 (> 100 h) at the low temperature of 90°C. This very short equilibration time emphasizes the point made above about laboratory time scales sufficient to destabilize QD heterostructures that are not thermodynamically stable, such as the ZnTe/ZnSe reverse core/shell initial configuration here.

Effects of Compositional Distribution on the Electronic Properties of Semiconductor Ternary Quantum Dots

To study the effects of the overall ternary nanocrystal composition and compositional distribution in the nanocrystal on the electronic and optical properties of the ternary QDs, we carried out detailed computations of the electronic structure of $ZnSe_{1-x}S_x$ and $ZnSe_{1-x}Te_x$ QDs. Specifically, in order to elucidate the importance of the compositional distribution in these ternary semiconductor nanocrystals, we analyzed various types of configurations ranging from completely randomly alloyed nanocrystals to core/shell QDs. Detailed results on the electronic structures of these various configurations have been reported in Refs. 36 and 37, including the wave function and charge density distributions, as well as the electronic densities of states. Here, we focus on the dependence in these nanocrystal configurations of the electronic band gap on the overall compositional parameter x, $E_g(x)$. Our findings identify the configurations that allow for optimal band-gap tunability.

For the determination and analysis of the electronic structure of the semiconductor ternary QDs examined, we carried out first-principles DFT calculations within the GGA according to the Perdew–Burke–Ernzerhof exchange and correlation functional.[25] At this theory level, we employed plane-wave basis sets for the expansion of the electronic wave functions and we used the PAW method[26,27] for the treatment of the ionic cores as implemented in the Vienna Ab initio Simulation Package (VASP).[23,24] Following systematic convergence tests, we chose a kinetic-energy cutoff of 280 eV for plane waves and used only the Γ point for **k**-point sampling in the irreducible wedge of the first Brillouin zone of the reciprocal lattice of the nanocrystal. The surface atoms of the QDs were passivated in the calculations; for passivation, in the tetrahedrally coordinated zinc-blende lattice, pseudo-hydrogen atoms were used with fractional nuclear charge of $(8 - m)/4$, where m is the valence charge of the surface atom.[38] In the cases addressed here, Se, S, and Te are isovalent elements ($m = 6$), requiring identical passivation for their surface dangling bonds. For a given compositional distribution in the QD, prior to the electronic structure analysis, the QD configurations examined were fully relaxed (through wave function, atomic-configuration geometry, and volume optimization) in a self-consistent manner. Due to the computational demands of this analysis, smaller QDs were used than those employed in the MC relaxation procedure presented above; specifically, we used QDs of size $d \sim 1.8$ nm, consisting of 163 atoms of Zn and group-VI elements together with the pseudo-H atoms used for surface bond passivation.

The results for the compositional dependence of the band gap, $E_g(x)$, for the various compositional distributions in the $ZnSe_{1-x}S_x$ QDs examined are shown in Figure 11a.

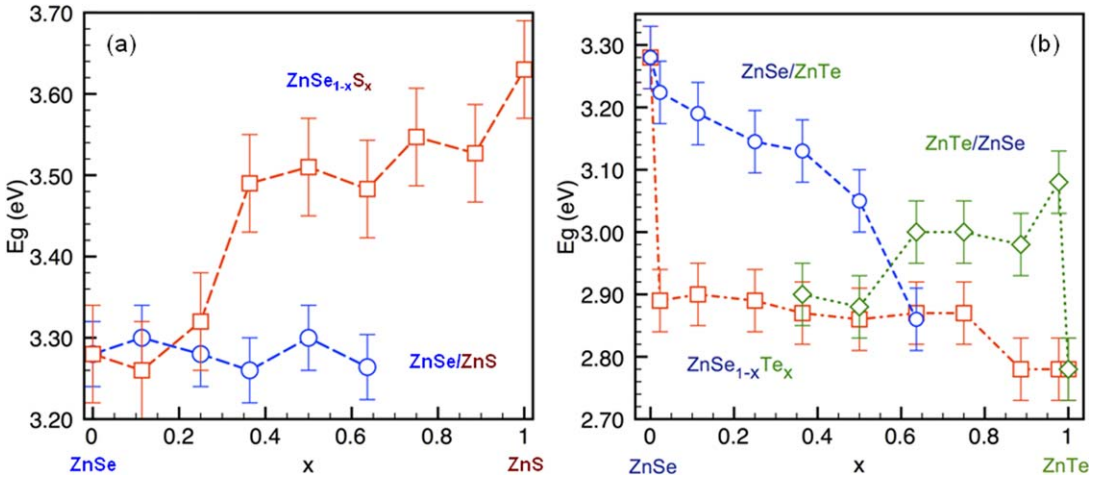

Figure 11. (a) Band gap, E_g, as a function of the S concentration, x, and its distribution in randomly alloyed $ZnSe_{1-x}S_x$ (open squares) and core/shell ZnSe/ZnS (open circles) QD configurations; (b) band gap, E_g, as a function of the Te concentration, x, and its distribution in ZnSe/ZnTe core/shell (open circles), ZnTe/ZnSe reverse core/shell (open diamonds), and alloyed $ZnSe_{1-x}Te_x$ (open squares) ternary QD configurations.

[Color figure can be viewed in the online issue, which is available at wileyonlinelibrary.com.]

Specifically, we calculated the electronic structure of the pristine (intrinsic) ZnSe QD, randomly alloyed $ZnSe_{1-x}S_x$ configurations consisting of a substitutional solid solution of S and Se, and ZnSe/ZnS core/shell configurations consisting of a ZnSe core coated with ZnS with a coating thickness ranging from partial-monolayer to one-monolayer thick (adjusted by varying x). The results of Figure 11a indicate that, in the core/shell configuration, the band gap is a weak function of the fraction x of S atoms among all group-VI atoms in the nanocrystal; in this configuration, increasing x leads from a partially covered core to a one-monolayer-thick ZnS shell. On the contrary, in the randomly alloyed $ZnSe_{1-x}S_x$ QD configuration, the band gap increases nonlinearly with x, exhibiting a strong dependence on x, $E_g(x)$. This implies that, during alloy formation, a significant shift occurs in the band gap of the intrinsic ZnSe QD with increasing the number of S atoms in the core; this occurs in conjunction with a decrease in the optical transition intensity. We already know that ZnSe/ZnS core/shell configurations are not thermodynamically stable and, during thermal annealing, transform to randomly alloyed configurations.[14,34] According to the results of Figure 11a, for a fixed total S content in the QD, the transition from the core/shell to the randomly alloyed configuration is accompanied by a shift in the electronic band gap of the QD; the quantitative value of this shift in E_g depends on the actual value of x (i.e., the actual number of S atoms involved in the transformation) and is ~0.2 eV for a one-monolayer-thick shell. This shift in the band gap of the QD is accompanied by a decrease in its optical intensity and provides a comprehensive interpretation to experimental observations of band edge luminescence in ZnSe/ZnS QDs with compositional control.[39] More importantly, the dependence of E_g on x in the randomly alloyed configuration implies that, in this configuration, the electronic band gap of the QD can be tuned by controlling the compositional parameter x.

Figure 11b shows our results for the compositional dependence of the electronic band gap, $E_g(x)$, for the various compositional distributions that we examined in $ZnSe_{1-x}Te_x$ QDs. In this case, we studied five types of nanocrystal configurations, namely, pristine (intrinsic) ZnSe and pristine ZnTe QDs, ZnSe/ZnTe core/shell and ZnTe/ZnSe reverse core/shell configurations, as well as randomly alloyed $ZnSe_{1-x}Te_x$ ternary QDs. It is evident that adding even a single Te atom in the QD core ($x \rightarrow 0$) has a significant impact on the band gap of the QD. In the randomly alloyed configuration, however, increasing the Te concentration beyond the dilute limit does not cause practically any change in the band gap until $x \sim 0.9$, where the dilute limit of Se is reached in the intrinsic ZnTe QD; in this limit, the change in E_g is less drastic (~0.1 eV) than in the dilute limit of Te ($x \sim 0.1$, where the shift in the band gap compared to that of pristine ZnSe is ~0.3 eV). This $E_g(x)$ behavior shows that, in randomly alloyed ternary QDs, Te acts as an isoelectronic dopant upon its introduction in the core of the QD. A smoother and stronger $E_g(x)$ dependence is exhibited in the ZnSe/ZnTe core/shell configuration, where the Te atoms are kept on the nanocrystal surface; this smooth monotonic decrease of the band gap with increasing Te concentration implies that in such core/shell configurations the band gap can be tuned precisely by controlling the compositional parameter x. A dependence of E_g on x intermediate between those of the core/shell and randomly alloyed configurations is exhibited in the ZnTe/ZnSe reverse core/shell configuration, where the Se atoms are kept on the nanocrystal surface. Also, it is evident that near the dilute limit $x \rightarrow 1$, addition of Se atoms to the ZnTe QD leads to an opposite behavior of the band gap compared to that of the ZnSe QD upon addition of Te atoms near the dilute limit $x \rightarrow 0$. In general, a change in the Te or Se concentration on the surface of the QD will lead to a significant shift in the band gap that will increase with increasing the number of Te atoms and decrease with increasing the number of Se atoms. In addition, for fixed x, changing the compositional distribution from a core/shell (or reverse core/shell) to a randomly alloyed one will cause a red shift in the photoluminescence emission energies of the QD due to the band-gap decrease involved in such a transformation with the exact shift determined by the exact value of x. A blue shift will be caused in the opposite transformation (from randomly alloyed to core/shell). The results of Figure 11b will be instrumental in interpreting future experimental measurements of photoluminescence

spectra of $ZnSe_{1-x}Te_x$ QDs with controlled Se or Te concentration.

For the generation of certain configurations in the ternary II–VI QDs examined, there are numerous possibilities for the occupation of the lattice sites of the nanocrystal or of its surface by the atoms of the two group-VI elements; such configurations include randomly alloyed configurations and low-x configurations consisting of partially grown shells on an original QD core and require systematic sampling of site occupation for determining their properties at certain composition. Due to the computationally demanding DFT/GGA calculations employed in this study, only a few possible configurations have been sampled; this limited sampling is the source of the error bars reported in the results of Figure 11. Also, it should be mentioned that DFT/GGA predictions of band gaps are well known to have quantitative errors. In this study, we have not corrected the E_g predictions by, for example, going to a higher-level DFT through a different type of functional in the calculations. We did not have to correct these predicted absolute values because we are only interested in the qualitative trends in the relevant shifts of the band gaps as a result of changes in the composition and its distribution in the QD; these are comparable irrespective of the type of functional used in the computations.

The discussion of the previous two sections has revealed that the thermodynamically stable configurations of $ZnSe_{1-x}S_x$ QDs are essentially randomly alloyed configurations, while the thermodynamically stable compositional distributions of $ZnSe_{1-x}Te_x$ QDs correspond to core/shell-like configurations with Te-deficient cores and Te-rich shells connected through a smooth graded interface. The results of Figure 11 imply that these thermodynamically stable configurations are the ones best suitable for precise tuning of the band gap by controlling the overall composition of the nanocrystal. The important implication is that carefully designed post-growth nanocrystal annealing, which leads to self-assembly of the thermodynamically (as opposed to kinetically) stable configurations, will generate ternary QDs with tunable band gaps. The optoelectronic properties of these QDs can, therefore, be controlled by tailoring the QD composition (i.e., the compositional parameter x) when the nanocrystals are grown; to optimize the growth and annealing processes, the nanocrystals should be grown at/near the thermodynamically controlled regime, where slower growth rates are achieved at low temperatures.

Summary and Conclusions

In summary, we analyzed the diffusional transport of atomic species in semiconductor ternary QDs driven by the tendency of certain species to segregate on the semiconductor nanocrystal surface. We developed a continuum transport model for such driven diffusional transport, validated it by comparisons of its predictions with those of first-principles-based atomic-scale simulations, and used it to fit experimental data and atomistic simulation results to develop a database of transport properties in ternary QDs. This database and the continuum model provide a valuable design tool for the development of thermal annealing processes that drive the assembly of core/shell-like structures from as grown QD configurations that may be kinetically locked at the low temperature of QD growth (by, e.g., colloidal synthesis techniques). Furthermore, we demonstrated the effects of different compositional distributions in ternary QDs with given overall content of their constituents on the electronic band gaps of the QDs.

Our findings have various important implications for the development of ternary QDs with optimal function in optoelectronic and photovoltaic devices. A critical implication is for the stability of QDs grown as core/shell heterostructures through a two-step growth process, where a QD core is grown and then coated by a shell of different composition from that of the core. Although such a heterostructure may have very promising optoelectronic properties, afforded due to the presence of the core/shell interface, it may be thermodynamically unstable. During further thermal processing of the QD or during its service in a high-temperature environment, species diffusion in the QD, driven by the tendency of certain QD constituents for surface segregation, will destabilize the original core/shell interface with dramatic consequences for the QD's electronic properties. Given the small diffusional length scales in the QDs ($d \sim 5$ nm) and any high temperatures that enhance significantly the rates of diffusional processes in crystalline lattices, such QD instabilities may be realized over short laboratory time scales (from a few seconds to many hours) and have severe effects on the QD-based devices.

Perhaps more importantly, we have found that QDs with thermodynamically stable compositional distributions have electronic band gaps that can be tuned precisely. This was demonstrated in this study for $ZnSe_{1-x}S_x$ and $ZnSe_{1-x}Te_x$ QDs, but our approach can be generalized to any ternary QD and preliminary results suggest the generality of this conclusion. In addition to the well-known capabilities for electronic property tuning in QDs by controlling their size, ternary QDs offer further advantages through control of their overall composition. Such compositional control is easy to accomplish during QD growth. Therefore, our study proposes an overall optimal yet simple strategy for growing ternary QDs with the required properties for the desired function in devices. This strategy consists of one-step growth processes, as opposed to multi-step processes for growing separate layers (core vs. shell), followed simply by self-assembly of the thermodynamically stable QD configuration aided properly by thermal annealing. Following such a strategy will have beneficial effects over a broad range of technological applications; for example, in QDs used in solar-cell architectures, it will lead to increased efficiency by optimizing absorption from the solar spectrum.

Acknowledgments

This work was supported by Polymer-Based Materials for Harvesting Solar Energy, an Energy Frontier Research Center funded by the U.S. Department of Energy (DOE), Office of Basic Energy Sciences under Award No. DE-SC0001087. DM also acknowledges support by the U.S. Department of Energy, Office of Fusion Energy Sciences and Office of Advanced Scientific Computing Research through the Scientific Discovery through Advanced Computing (SciDAC) project on Plasma Surface Interactions, funded by Award No. DE-SC0008875 (development of theory for drift mass transport).

Literature Cited

1. Pandey SC, Mountziaris TJ, Venkataraman D, Maroudas D. Formation of core/shell-like $ZnSe_{1-x}Te_x$ nanocrystals due to equilibrium surface segregation. *Appl Phys Lett*. 2010;96:201910/1–3.

2. Pandey SC, Maroudas D. Equilibrium compositional distribution in freestanding ternary semiconductor quantum dots: the case of $In_xGa_{1-x}As$. *J Chem Phys*. 2011;135:234701/1–12.
3. Lomascolo M, Creti A, Leo G, Vasanelli L, Manna L. Exciton relaxation processes in colloidal core/shell ZnSe/ZnS nanocrystals. *Appl Phys Lett*. 2003;82:418–420.
4. Hines MA, Guyot-Sionnest P. Synthesis and characterization of strongly luminescing ZnS-capped CdSe nanocrystals. *J Phys Chem*. 1996;100:468–471.
5. Dabbousi BO, Rodriguez-Viejo J, Mikulec FV, Heine JR, Mattoussi H, Ober R, Jensen KF, Bawendi MG. (CdSe)ZnS core-shell quantum dots: synthesis and characterization of a size series of highly luminescent nanocrystallites. *J Phys Chem B*. 1997;101: 9463–9475.
6. Peng XG, Schlamp MC, Kadavanich AV, Alivisatos AP. Epitaxial growth of highly luminescent CdSe/CdS core/shell nanocrystals with photostability and electronic accessibility. *J Am Chem Soc*. 1997; 119:7019–7029.
7. Kim S, Fisher B, Eisler HJ, Bawendi M. Type-II quantum dots: CdTe/CdSe(core/shell) and CdSe/ZnTe(core/shell) heterostructures. *J Am Chem Soc*. 2003;125:11466–11467.
8. Talapin DV, Mekis I, Gotzinger S, Kornowski A, Benson O, Weller H. CdSe/CdS/ZnS and CdSe/ZnSe/ZnS core-shell-shell nanocrystals. *J Phys Chem B*. 2004;108:18826–18831.
9. Reiss P. ZnSe based colloidal nanocrystals: synthesis, shape control, core/shell, alloy, and doped systems. *New J Chem*. 2007;31: 1843–1852.
10. Reiss P, Protiere M, Li L. Core/shell semiconductor nanocrystals. *Small*. 2009;5:154–168.
11. Cao Y, Banin U. Growth and properties of semiconductor core/shell nanocrystals with InAs cores. *J Am Chem Soc*. 2000;122:9692–9702.
12. Smith AM, Mohs AM, Nie S. Tuning the optical and electronic properties of colloidal nanocrystals by lattice strain. *Nat Nanotechnol*. 2009;4:56–63.
13. Wang X, Ren X, Kahen K, Hahn MA, Rajeswaran M, Zacher SM, Silcox J, Cragg GE, Efros AL, Krauss TD. Non-blinking semiconductor nanocrystals. *Nature*. 2009;459:686–689.
14. Han X, Pandey SC, Maroudas D. Kinetics of interdiffusion in semiconductor ternary quantum dots. *Appl Phys Lett*. 2012;101:141906/ 1–5.
15. Pandey SC, Sfyris GI, Maroudas D. Theory of surface segregation in ternary semiconductor quantum dots. *Appl Phys Lett*. 2011;98: 091907/1–3.
16. Bacon DJ. Mechanical interaction of a point defect with a surface-layer. *Physica Status Solidi B*. 1972;50:607.
17. Michel B. Influence of solid surfaces on the interaction energy of point defects. *Physica Status Solidi B*. 1977;81:K87–K90.
18. Maradudin AA, Wallis RF. Elastic interactions of point defects in a semi-infinite medium. *Surf Sci*. 1980;91:423–439.
19. Hirth JP, Lothe J. Theory of dislocations, 2nd ed. New York: Wiley, 1982.
20. Pandey SC. Modeling of growth and prediction of properties of electronic nanomaterials: silicon thin films and compound semiconductor quantum dots. PhD Dissertation, University of Massachusetts, Amherst, 2011.
21. Deen WM. Analysis of transport phenomena, 1st ed. Oxford: Oxford University Press, 1998.
22. Cottrell AH, Jawson MA. Distribution of solute atoms round a slow dislocation. *Proc R Soc Lond Series A*. 1949;199:104–114.
23. Kresse G, Furthmuller J. Efficient iterative schemes for ab initio total-energy calculations using a plane-wave basis set. *Phys Rev B*. 1996;54:11169–11186.
24. Kresse G, Furthmuller J. Efficiency of ab-initio total-energy calculations for metals and semiconductors using a plane-wave basis set. *Comput Mater Sci*. 1996;6:15–50.
25. Perdew JP, Burke K, Ernzerhof M. Generalized gradient approximation made simple. *Phys Rev Lett*. 1996;77:3865–3868.
26. Blöchl PE. Projector augmented-wave method. *Phys Rev B*. 1994;50: 17953–17979.
27. Kresse G, Joubert D. From ultrasoft pseudopotentials to the projector augmented-wave method. *Phys Rev B*. 1999;59:1758–1775.
28. Keating PN. Effect of invariance requirements on the elastic strain energy of crystals with application to the diamond structure. *Phys Rev*. 1966;145:637–645.
29. Martin RM. Elastic properties of ZnS structure semiconductors. *Phys Rev B*. 1970;1:4005–4011.
30. Martins JL, Zunger A. Bond lengths around isovalent impurities and in semiconductor solid solutions. *Phys Rev B*. 1984;30:6217–6220.
31. Foiles SM. Calculation of the surface segregation of Ni–Cu alloys with the use of the embedded-atom method. *Phys Rev B*. 1985;32: 7685–7693.
32. Kelires PC, Tersoff J. Equilibrium alloy properties by direct simulation: oscillatory segregation at the Si-Ge(100) 2×1 surface. *Phys Rev Lett*. 1989;63:1164–1167.
33. Balluffi RW, Granato AV. Dislocations, vacancies, and interstitials. In: Nabarro FRN, editor. Dislocations in solids, Vol. 4. Amsterdam: North Holland, 1979:1.
34. Pandey SC, Wang J, Mountziaris TJ, and Maroudas D. Thermodynamic instability of ZnSe/ZnS core/shell quantum dots. *J Appl Phys*. 2012;111:113526/1–8.
35. Finlayson BA. Nonlinear analysis in chemical engineering. New York: McGraw-Hill, 1980.
36. Pandey SC, Mountziaris TJ, Maroudas D. Compositional effects on the electronic structure of $ZnSe_{1-x}S_x$ ternary quantum dots. *Appl Phys Lett*. 2011;99:101902/1–3.
37. Pandey SC, Maroudas D. Effects of composition and compositional distribution on the electronic structure of $ZnSe_{1-x}Te_x$ ternary quantum dots. *J Appl Phys*. 2011;110:123509/1–6.
38. Huang X, Lindgren E, Chelikowsky JR. Surface passivation method for semiconductor nanostructures. *Phys Rev B*. 2005;71: 165328/1–6.
39. Lad AD, Mahamuni S. Effect of ZnS shell formation on the confined energy levels of ZnSe quantum dots. *Phys Rev B*. 2008;78:125421/ 1–8.

Manuscript received Dec. 17, 2012, and revision received Apr. 2, 2013.